# Conjugate Effects on Steady Laminar Natural Convection Heat Transfer in Vertical Eccentric Annuli

Maged A. I. El-Shaarawi
Esmail M. A. Mokheimer*
Ahmad Jamal

Mechanical Engineering Department, King Fahd University of Petroleum and Minerals, Dhahran, Saudi Arabia

Combined conduction-free convection heat transfer in vertical eccentric annuli is numerically investigated using finite-difference technique. Numerical results are presented for a fluid of Prandtl number 0.7 in an annulus of radius ratio 0.5 and dimensionless eccentricity 0.5. The conjugation effect on the induced flow rate and the total heat absorbed in the annulus is presented for the case of one wall being isothermally heated while the other wall is kept at inlet fluid temperature. The conjugate effects are controlled by solid-fluid conductivity ratio, cylinder walls thickness and dimensionless channel height (i.e. Grashof number). Solid-fluid conductivity ratio is varied over a range that covers practical cases with commonly encountered inner and outer walls thickness. Values of conductivity ratio over which conjugate effect can be neglected have been obtained.

* On leave from Ain Shams University, Cairo, Egypt.

**NOMENCLATURE**

| | |
|---|---|
| $a$ | Location of the positive pole of the bipolar coordinate system on the x-axis of the Cartesian coordinate system (constant in the bipolar transformation equations, equal to $r_i$ *sinh* $\eta_i$ or $r_o$ *sinh* $\eta_o$), m |
| $c_p$ | Specific heat of fluid at constant pressure, kJ/kg K |
| $D_h$ | Hydraulic or equivalent diameter of annulus, $2(r_{io} - r_{oi}) = 2a(1 - NR_2)\cos ech\,\eta_o$, m |
| $e$ | Eccentricity (distance between the axes of the two cylinders forming the eccentric annulus), $a$ (*coth* $\eta_o$ – *coth* $\eta_i$), m |
| $E$ | Dimensionless eccentricity, $\frac{e}{(r_{io} - r_{oi})}$ |
| $F$ | Dimensionless volumetric flow rate, $F = U_o\left(1 - NR_2{}^2\right)$ |
| $g$ | Gravitational body force per unit mass (acceleration), m/s$^2$ |
| $Gr$ | Grashof number, $\frac{g\beta(T_w - T_o)D_h{}^3}{\gamma^2}$ |
| $Gr^*$ | Modified Grashof number, $\frac{GrD_h}{l}$ |
| $h$ | Coordinate transformation scale factor, m |
| $H$ | Dimensionless coordinate transformation scale factor, $\frac{h}{D_h}$ |
| $HF_{i,ex}$ | Dimensionless Local heat flux on inner interface at channel exit |
| $HF_{o,ex}$ | Dimensionless Local heat flux on outer interface at channel exit |
| $i$ | Index for bi-polar grid in the η-direction and the cylindrical grid in the radial direction |
| *Iwall* | Dimensionless thickness of inner cylinder wall, $NR_2$-$NR_1$ |
| $j$ | Index for the bi-polar grid in the ξ-direction and the cylindrical grid in the tangential direction |
| $K_f$ | Thermal conductivity of fluid, W/m.K |
| $K_s$ | Thermal conductivity of solid, W/m.K |
| $KR$ | Solid-fluid conductivity ratio, $K_s/K_f$ |
| $l$ | Height of the channel, m |
| $L$ | Dimensionless height of channel (value of $Z$ at channel exit), $1/Gr^*$ |
| $M$ | Number of intervals in each of the $\xi$ & $\phi$ directions |
| $N$ | Number of intervals in the $\eta$-direction |
| $NR_1$ | Ratio between inner radius of inner cylinder and inner radius of outer cylinder, $\frac{r_{ii}}{r_{io}}$ |

$NR_2$ Ratio between outer radius of inner cylinder and inner radius of outer cylinder (Fluid annulus radius ratio), $\frac{r_{oi}}{r_{io}}$

$NR_3$ Dimensionless inner radius of outer cylinder, $\frac{r_{io}}{r_{io}} = 1$

$NR_4$ Ratio between outer radius of outer cylinder and inner radius of outer cylinder, $\frac{r_{oo}}{r_{io}}$

$NSI$ Number of radial intervals in the inner cylinder wall

$NSO$ Number of radial intervals in the outer cylinder wall

$NU_{i,ex}$ Nusselt number on inner interface at channel exit

$NU_{o,ex}$ Nusselt number on outer interface at channel exit

$Owall$ Dimensionless thickness of outer cylinder wall, $NR_4$-$NR_3$

$p$ Pressure of fluid inside the channel at any cross-section, N/m$^2$

$P$ Dimensionless Pressure defect of fluid inside the channel at any cross section, $\frac{P' D_h{}^4}{\rho l^2 \gamma^2 Gr*^2}$

$P_0$ Dimensionless inlet fluid pressure, $-\frac{U_0{}^2}{2}$

$p_s$ Hydrostatic pressure, $\rho g z$, N/m$^2$

$p'$ Pressure defect at any point, $p - p_s$, N/m$^2$

$\overline{Q}$ Dimensionless heat absorbed up to the annulus exit, i.e., values of $Q$ at $z$ = l, $F\theta_{m,ex}$

$r_{ii}$ Inner radius of inner cylinder, m

$r_{oi}$ Outer radius of inner cylinder, m

$r_{io}$ Inner radius of outer cylinder, m

$r_{oo}$ Outer radius of outer cylinder, m

$R$ Dimensionless radial coordinate, $\frac{r}{r_{io}}$

$\Delta R_i$ $\frac{NR_2 - NR_1}{NSI}$

$\Delta R_o$ $\frac{NR_4 - NR_3}{NSO}$

$T_o$ Ambient or fluid entrance temperature, K

$T_w$ Isothermal temperature of heated wall, K

$u$ Axial (stream wise) velocity component, m/s

$U$ Dimensionless axial velocity at any point, $\frac{u r_{io}{}^2}{l \gamma Gr*}$

$U_o$ Dimensionless axial velocity at annulus entrance, $\frac{u_o r_{io}^{\ 2}}{l\gamma Gr^*}$

$v$ $\eta$-velocity component, m/s

$V$ Velocity vector or dimensionless $\eta$-velocity component, $\frac{vD_h}{\gamma}$

$w$ $\xi$-velocity component, m/s

$W$ Dimensionless $\xi$-velocity component, $\frac{wD_h}{\gamma}$

$z$ Axial coordinate in both the Cartesian and bipolar coordinate systems, m

$Z$ Dimensionless axial coordinate in both the Cartesian and bipolar coordinate systems, $\frac{z}{lGr^*}$

$Z_{,ex}$ Value of Z at channel exit

$\Delta Z$ Dimensionless axial step increment, $\frac{\Delta z}{lGr^*}$

*Greek Letters*

$\beta$ Volumetric coefficient of thermal expansion, $K^{-1}$

$\eta$ First transverse bi-polar coordinate

$\eta_i$ Value of $\eta$ on the inner interface,

$$\eta_i = \log_e\left[\frac{NR_2\left(1+E^2\right)+\left(1-E^2\right)}{2NR_2E}+\sqrt{\left(\frac{NR_2\left(1+E^2\right)+\left(1-E^2\right)}{2NR_2E}\right)^2-1}\right]$$

$\eta_o$ Value of $\eta$ on the outer interface,

$$\eta_o = \log_e\left[\frac{NR_2\left(1-E^2\right)+\left(1+E^2\right)}{2E}+\sqrt{\left(\frac{NR_2\left(1-E^2\right)+\left(1+E^2\right)}{2E}\right)^2-1}\right]$$

$\Delta\eta$ Numerical grid mesh size in $\eta$-direction, $\frac{\eta_i-\eta_o}{N}$

$\theta$ Dimensionless temperature, $\frac{\left(T-T_o\right)}{\left(T_w-T_o\right)}$ for isothermal walls case

$\theta_f$ Value of $\theta$ in the fluid annulus

$\theta_{m,ex}$ Mean bulk temperature at channel exit

$\theta_{si}$ Value of $\theta$ in the inner solid wall

$\theta_{so}$ Value of $\theta$ in the outer solid wall.

$\mu$ Dynamic viscosity of fluid, $N.s/m^2$

$\gamma$ Kinematic viscosity of fluid, $\frac{\mu}{\rho}$ , $m^2/sec$

$\rho$ Density of Fluid, kg/m$^3$

$\Psi$ Normalized value of $\xi$, $\frac{\xi}{\pi}$

$\alpha$ Thermal diffusivity of fluid, $\frac{k}{\rho c_p}$, m$^2$/sec

$\xi$ Second transverse bi-polar coordinate

$\Delta\xi$ Numerical grid mesh size in $\xi$-direction, $\frac{\pi}{M}$

$\phi$ Angle along the cylinder walls

$\Delta\phi$ Numerical grid mesh size in $\phi$-direction, $\frac{\pi}{M}$

**Introduction**

The study of steady laminar induced flow in vertical eccentric annuli with conjugate heat transfer is of great importance because of its many engineering applications in electrical, nuclear, solar and thermal storage fields. A typical application is that of gas cooled nuclear reactor, in which cylindrical fissionable fuel elements are placed axially in vertical coolant chambers within the graphite moderator; the cooling gas is flowing along the channel parallel to the fuel element. In such a system, laminar free convection may provide the sole means of the necessary cooling during the shut down or accident periods.

In conventional heat transfer analyses, one of the common practices is to prescribe the temperature at the fluid-wall interface. Consequently, the energy equation of the fluid alone has to be solved. The results thus obtained are good only for heat transfer in flows bounded by walls having extremely small thermal resistance, i.e. very high thermal conductivity and/or very small thickness. However, in actual practice, the wall thermal resistance is finite and consequently the temperature at the fluid-wall interface is different from that imposed at the other surface of the solid wall. Such type of problems, where heat conduction in the solid is coupled with convective heat transfer in the fluid, is often referred to as conjugate problems. If the bounding cylinder walls are thick and have low thermal conductivity, conjugation (coupling of conduction and convection) must be taken into account as it can significantly affect the heat transfer.

Considerable work has been done to study the problem of flow and conjugate heat transfer in various geometries and annuli, both concentric and eccentric. Anand and Tree [1] studied the effect of axial conduction in a tube wall on the steady-state laminar convective heat transfer. Kim and Anand [2] numerically investigated the effect of wall conduction on the free convection between asymmetrically heated vertical plates with uniform wall heat flux. Kim et al.

[3] numerically studied laminar free convection heat transfer in channels formed between series of vertical parallel plates with an embedded line heat source. Sakikabara et al. [4], analytically, investigated the steady conjugate heat transfer problem in an annulus with a heated core and an insulated outside tube when the laminar flow is hydrodynamically fully developed. El-Shaarawi et al. [5] presented a finite-difference scheme to solve the transient conjugate forced convection in a concentric annulus with simultaneously developing hydrodynamic and thermal boundary layers. Using finite-difference technique, El-Shaarawi and Negm [6] solved the laminar conjugate natural convection problem in vertical open-ended concentric annuli. Shu and Wu [7] developed a numerical approach, the Domain Free Discretization (DFD), to simulate natural convection in an eccentric annulus.

Similarly, in spite of the many studies reported in the literature for the conventional case of convection in annuli [8-16], the only work available for the conjugate case is that of El-Shaarawi and Haider [17] for forced convection. They presented results for a fluid of Prandtl number 0.7 flowing in an annulus of radius ratio $NR_2$=0.5 with $E$=0.1, 0.3, 0.5 and 0.7.

A thorough literature survey revealed that conjugate natural convection heat transfer in vertical eccentric annuli has not been investigated yet. The present paper presents a numerical algorithm, employing finite-difference technique, to solve the boundary layer model for this problem. Numerical results are presented for the conjugation effect on the induced flow rate and heat transfer under two thermal boundary conditions. In each of these two boundary conditions there is one surface maintained at a prescribed temperature other than the inlet fluid temperature while the other surface is kept at the inlet fluid temperature.

## Governing Equations

Figure 1(a) depicts two dimensional cross-section plan and elevation of the geometry under consideration. Bipolar coordinate system is used to express the partial differential equations describing the flow and heat transfer through the eccentric fluid annulus. The cylinder walls have uniform thickness. Hence, the cylindrical coordinate system is more appropriate for the solid walls. So, the energy equation for the solid walls will be expressed in cylindrical coordinates.

The vertical eccentric annulus of finite height is open at both ends and immersed in a stagnant Newtonian fluid of infinite extent maintained at constant temperature $T_o$. Free convection flow is induced inside this annular channel as a result of heating one of the channel walls isothermally while keeping the other wall at ambient temperature $T_o$. Thus two cases are under investigation. One is named case (I) in which the heated wall is the inner cylinder whereas

the other is called case (O) in which the heated wall is the outer cylinder. The fluid entering the channel at the ambient temperature $T_o$ obeys the Boussinesq approximation, according to which its density is allowed to vary with temperature in only the gravitational body force term of the vertical (axial) momentum equation. Since the eccentric annular geometry is symmetric about line AB, one half of the symmetric section is considered in the solution. Figure 1(b) shows the 2-D cross-section of that half.

The fluid is assumed to be Newtonian with constant physical properties. The flow is steady, laminar, enters the eccentric annulus with a velocity ($U_o$) and then development of its hydrodynamic and thermal boundary layers occurs. Body forces in other than the vertical direction, viscous dissipation, internal heat generation and radiation heat transfer are absent. The governing equations describing the flow and heat transfer through the eccentric fluid annulus are as follows.

*Continuity Equation*

$$\nabla . V = 0 \tag{1}$$

*Momentum Equation*

$$\rho \frac{DV}{Dt} = F - \nabla P + \mu \nabla^2 V \tag{2}$$

*Energy Equation*

$$\rho c_p \frac{DT}{Dt} = k \nabla^2 T + Q''' + \mu \Phi \tag{3}$$

Hughes and Gaylord [18] gave these governing equations in a general orthogonal curvilinear coordinate system. However, as previously stated, bipolar coordinate system is used to express the partial differential equations describing the flow and heat transfer through the eccentric fluid annulus. This bi-polar coordinate system is as shown in Fig. 1(c). Moreover, some parabolic-flow assumptions [16] will be used to simplify the model comprising of these governing equations. These assumptions include: the pressure is a function of the axial coordinate only ($\frac{\partial p}{\partial \eta} = \frac{\partial p}{\partial \xi} = 0$), the axial diffusions of momentum and energy in the axial ($z$) direction are neglected ($\frac{\partial^2}{\partial z^2} = 0$), and the $\eta$-velocity component ($v$) is much smaller than $\xi$ and $z$-velocity components ($w$ and $u$). Carrying out the order of magnitude analysis, taking into

consideration that the latter assumption results in dropping the $\eta$-momentum equation, and introducing the dimensionless parameters given in the nomenclature, the governing equations, for a steady flow without internal heat generation ($Q''' = 0$), negligible viscous dissipation ($\Phi = 0$) and body force ($F$) in the vertical direction, can be written in the following dimensionless forms.

*Continuity Equation*

$$\frac{\partial(HW)}{\partial\xi} + \frac{\partial(HV)}{\partial\eta} + 4(1-NR_2)^2\frac{\partial\left(UH^2\right)}{\partial Z} = 0 \tag{4}$$

*Momentum Equation In Z-Direction*

$$\frac{W}{H}\frac{\partial U}{\partial\xi} + \frac{V}{H}\frac{\partial U}{\partial\eta} + 4(1-NR_2)^2 U\frac{\partial U}{\partial Z} = \frac{\theta}{4(1-NR_2)^2} - \frac{1}{4(1-NR_2)^2}\frac{\partial P}{\partial Z} + \frac{1}{H^2}\left(\frac{\partial^2 U}{\partial\xi^2} + \frac{\partial^2 U}{\partial\eta^2}\right) \tag{5}$$

*Momentum Equation In $\xi$-Direction*

$$\frac{W}{H}\frac{\partial W}{\partial\xi} + \frac{V}{H^2}\frac{\partial(HW)}{\partial\eta} + 4(1-NR_2)^2 U\frac{\partial W}{\partial Z} - \frac{V^2}{H^2}\frac{\partial H}{\partial\xi} = \frac{1}{H^3}\left[\frac{\partial^2(HW)}{\partial\eta^2} + \frac{\partial^2(HW)}{\partial\xi^2}\right] - \frac{2}{H^4}\left[\frac{\partial(HW)}{\partial\eta} - \frac{\partial(HV)}{\partial\xi}\right]\frac{\partial H}{\partial\eta} + \frac{8(1-NR_2)^2}{H^2}\frac{\partial H}{\partial\xi}\frac{\partial U}{\partial Z} \tag{6}$$

*Energy Equation for Fluid*

$$\frac{W}{H}\frac{\partial\theta}{\partial\xi} + \frac{V}{H}\frac{\partial\theta}{\partial\eta} + 4\left(1-NR_2\right)^2 U\frac{\partial\theta}{\partial Z} = \frac{1}{\mathrm{Pr}\,H^2}\left(\frac{\partial^2\theta}{\partial\eta^2} + \frac{\partial^2\theta}{\partial\xi^2}\right) \tag{7}$$

As each cylinder wall has uniform thickness, the cylindrical coordinate system is more appropriate for writing the governing energy equation in each of these solid walls. So, the energy equation for each of the solid walls in cylindrical coordinate system is as follows:

*Energy Equation for Solid Walls*

$$\frac{\partial^2\theta_s}{\partial R^2} + \frac{1}{R}\frac{\partial\theta_s}{\partial R} + \frac{1}{R^2}\frac{\partial^2\theta_s}{\partial\phi^2} = 0 \tag{8}$$

For outer cylinder, $\theta_s = \theta_{so}$ & $R$ vary from $NR_3$=1 to $NR_4$ and for inner cylinder, $\theta_s = \theta_{si}$ & $R$ vary from $NR_1$ to $NR_2$.

It is worth mentioning that the bi-polar coordinate system has been used to describe the flow and heat transfer in the eccentric fluid annulus. In this bipolar coordinate system the boundary surfaces of the fluid annulus are taken as one of the coordinates (η) and the other coordinate (ξ) comprises a set of eccentric annuli whose centers lie on the y-axis and orthogonally intersect the boundaries of the fluid annulus. However, since the cylinder solid walls have uniform thickness, the cylindrical coordinate system is more appropriate for these solid walls. Therefore, the energy equation for each of the inner and outer solid cylinder walls is expressed in cylindrical coordinate. Continuity of temperature and heat flux at the solid fluid interfaces provides the necessary link. The use of two coordinate systems rather than one was proven to be successful in describing the conjugate problem for the forced convection case [17] and consequently has been applied in the present free convection case. Thus, the bi-polar coordinate system has been used in writing the energy equation (7) for the fluid region as this coordinate system best suits the eccentric fluid annulus. On the other hand, the cylindrical polar coordinate system has been used in writing the energy equation (8) for each concentric solid annular region.

The continuity equation (4) subject to the no-slip conditions at the walls can be written in the following integral form.

*Integral Form of the Continuity Equation*

$$\overline{U} = \frac{8(1-NR_2)}{\pi(1+NR_2)} \int_0^{\pi} \int_{\eta_o}^{\eta_i} UH^2 \, d\eta \, d\xi \qquad (9)$$

Equations (4) through (8) are subject to the following boundary conditions:

- For $Z = 0$ and $\eta_o < \eta < \eta_i$ , $V = W = 0$ , and $U = U_o$ , $P = -U_o^2/2$
- For $Z = L$ and $\eta_o < \eta < \eta_i$ , $P = 0$
- For $Z \geq 0$ and $\eta = \eta_i$ or $\eta = \eta_o$ , , $U = V = W = 0$
- For case (I), $\theta_{si} = 1.0$ and $\theta_{so} = 0.0$ and for case (O), $\theta_{si} = 0.0$ and $\theta_{so} = 1.0$
- For $Z > 0$ and $\xi = 0$ and $\pi$ (the line of symmetry):

  $$\frac{\partial V}{\partial \xi} = \frac{\partial W}{\partial \xi} = \frac{\partial U}{\partial \xi} = \frac{\partial \theta}{\partial \xi} = \frac{\partial \theta_s}{\partial \phi} = 0$$

- For $Z > 0$ and $R = NR_2$ and $R = NR_3 = 1$ (i.e. the interfaces)

  $\theta_f = \theta_s$ , continuity of temperature, and

$k_f \left( \frac{1}{H}\frac{\partial \theta}{\partial \eta} i + \frac{1}{H}\frac{\partial \theta}{\partial \xi} j \right) = k_s \left( \frac{\partial \theta_s}{\partial R} i + \frac{1}{R}\frac{\partial \theta_s}{\partial \phi} j \right)$ , continuity of heat flux, where

$i$ , unit vector in the $\eta$ and $R$ directions

$j$ , unit vector in the $\xi$ and $\phi$ directions

**Numerical Analysis**

The above governing equations are numerically treated using a finite-difference technique to solve for the three velocity components, pressure and temperature in the fluid field and for the temperature in the two solid cylinders. Using backward finite-difference to express all first derivatives with respect to $Z$ and the first derivative of ($HV$) with respect to $\eta$ in the continuity equation and replacing the second and other first order derivatives in $\eta$ and $\xi$ directions by central finite-differences, equations (4) through (9) can be written in the following forms:

*Continuity Equation*

$$\frac{H(i,j+1)\,W(i,j+1) - H(i,j-1)\,W(i,j-1)}{2\Delta\xi} + \frac{H(i,j)\,V(i,j) - H(i-1,j)\,V(i-1,j)}{\Delta\eta} + 4(1-NR_2)^2 H^2(i,j)\frac{U(i,j) - U^*(i,j)}{\Delta Z} = 0 \tag{10}$$

*Z-Momentum Equation*

$$\frac{W^*(i,j)}{H(i,j)}\frac{U(i,j+1) - U(i,j-1)}{2\Delta\xi} + \frac{V^*(i,j)}{H(i,j)}\frac{U(i+1,j) - U(i-1,j)}{2\Delta\eta} + 4(1-NR_2)^2 U^*(i,j)\frac{U(i,j) - U^*(i,j)}{\Delta Z} = -\frac{1}{4(1-NR_2)^2}\frac{P(i,j) - P^*(i,j)}{\Delta Z} + \frac{\theta_f}{4(1-NR_2)^2} + \frac{1}{[H(i,j)]^2}\left[\frac{U(i-1,j) - 2U(i,j) + U(i+1,j)}{(\Delta\eta)^2} + \frac{U(i,j-1) - 2U(i,j) + U(i,j+1)}{(\Delta\xi)^2}\right] \tag{11}$$

*ξ-Momentum Equation*

$$\frac{W^*(i,j)}{H(i,j)}\frac{W(i,j+1)-W(i,j-1)}{2\Delta\xi}+\frac{V^*(i,j)}{(H(i,j))^2}\frac{H(i+1,j)W(i+1,j)-H(i-1,j)W(i-1,j)}{2\Delta\eta}$$
$$+4(1-NR_2)^2U^*(i,j)\frac{W(i,j)-W^*(i,j)}{\Delta Z}-\frac{(V^*(i,j))^2}{(H(i.j))^2}\frac{H(i.j+1)-H(i,j-1)}{2\Delta\xi}$$
$$=\frac{1}{(H(i,j))^3}\left\{\begin{array}{l}\dfrac{H(i-1,j)W(i-1,j)-2H(i,j)W(i,j)+H(i+1,j)W(i+1,j)}{(\Delta\eta)^2}\\+\dfrac{H(i,j-1)W(i,j-1)-2H(i,j)W(i,j)+H(i,j+1)W(i,j+1)}{(\Delta\xi)^2}\end{array}\right\} \quad (12)$$
$$-\frac{2}{(H(i,j))^4}\left(\frac{H(i+1,j)-H(i-1,j)}{2\Delta\eta}\right)\left\{\begin{array}{l}\dfrac{H(i+1,j)W(i+1,j)-H(i-1.,j)W(i-1,j)}{2\Delta\eta}\\-\dfrac{H(i,j+1)V(i,j+1)-H(i,j-1)V(i,j-1)}{2\Delta\xi}\end{array}\right\}$$
$$+\frac{8(1-NR_2)^2}{(H(i,j))^2}\frac{H(i,j+1)-H(i,j-1)}{2\Delta\xi}\frac{U(i,j)-U^*(i,j)}{\Delta Z}$$

*Energy Equation for Fluid*

$$\frac{W^*(i,j)}{H(i,j)}\frac{\theta_f(i,j+1)-\theta_f(i,j-1)}{2\Delta\xi}+\frac{V^*(i,j)}{H(i,j)}\frac{\theta_f(i+1,j)-\theta_f(i-1,j)}{2\Delta\eta}+$$
$$4(1-NR_2)^2U^*(i,j)\frac{\theta_f(i,j)-\theta_f{}^*(i,j)}{\Delta Z}=\frac{1}{\mathrm{Pr}(H(i,j))^2}\left(\begin{array}{l}\dfrac{\theta_f(i-1,j)-2\theta_f(i,j)+\theta_f(i+1,j)}{(\Delta\eta)^2}+\\\dfrac{\theta_f(i,j-1)-2\theta_f(i,j)+\theta_f(i,j+1)}{(\Delta\xi)^2}\end{array}\right) \quad (13)$$

*Energy Equation for Outer Solid Wall*

$$\frac{\theta_{so}(i+1,j)-2\theta_{so}(i,j)+\theta_{so}(i-1,j)}{(\Delta R_o)^2}+\frac{1}{[NR_4-(i-1)\Delta R_o]}\frac{\theta_{so}(i+1,j)-\theta_{so}(i-1,j)}{2\Delta R_o}$$
$$+\frac{1}{[NR_4-(i-1)\Delta R_o]^2}\frac{\theta_{so}(i,j+1)-2\theta_{so}(i,j)+\theta_{so}(i,j-1)}{(\Delta\phi)^2}=0 \quad (14)$$

*Energy Equation for Inner Solid Wall*

$$\frac{\theta_{si}(i+1,j)-2\theta_{si}(i,j)+\theta_{si}(i-1,j)}{(\Delta R_i)^2}+\frac{1}{[NR_2-(i-1)\Delta R_i]}\frac{\theta_{si}(i+1,j)-\theta_{si}(i-1,j)}{2\Delta R_i}$$
$$+\frac{1}{[NR_2-(i-1)\Delta R_i]^2}\frac{\theta_{si}(i,j+1)-2\theta_{si}(i,j)+\theta_{si}(i,j-1)}{(\Delta\phi)^2}=0 \quad (15)$$

*Integral Form of the Continuity Equation*

$$\overline{U}=\frac{8(1-NR_2)}{\pi(1+NR_2)}\left(\begin{array}{l}\displaystyle\sum_{j=2}^{M}\sum_{i=2}^{N}U(i,j)(H(i,j))^2+0.5\sum_{i=2}^{N}U(i,1)(H(i,1))^2+\\U(i,M+1)(H(i,M+1))^2\end{array}\right)\Delta\eta\Delta\xi \quad (16)$$

The finite-difference equations (10) through (12) are linearized by assuming that, where ever the product of two unknowns occurs, one of them is given approximately by its value at the previous axial step, the variable subscripted with an asterisk (*). Moreover, in Eq. (12), the finite difference representation of the $\xi$-momentum Eq. (6), all the values of $V$ have been deliberately taken at the previous axial step in order to make this equation locally (i.e. within one axial step) uncoupled from the continuity Eq. (10) and make the finite-difference Eqs. (10-16) represent a complete mathematical model of seven equations in seven unknowns ($U$, $V$, $W$, $P$, $\theta_f$, $\theta_{si}$, $\theta_{so}$); hence enable these equations to be numerically solved in the manner described later in this section. The dependent variables ($U$, $V$, $W$, $P$, $\theta_f$, $\theta_{si}$, $\theta_{so}$) are computed, for each axial (vertical) location ($Z$) at the intersections of the grid lines, i.e., the mesh points. The solution proceeds from the entrance of the channel to its exit in axial steps, the size of which increases exponentially.

Thermal boundary conditions are imposed on the inner surface of the inner cylinder and the outer surface of the outer cylinder. The thermal conditions at the two fluid-wall interfaces are not known. These thermal conditions depend on the thermal properties and flow characteristics of the fluid as well as the dimensions and properties of the solid walls. Having the governing equations for the fluid in bipolar coordinates and the energy equations for the solid walls in cylindrical coordinates generates unmatched grid points on both the interfaces. However, these points can be linked to determine the temperatures at the two interfaces by applying the principles of continuity of temperature and continuity of heat flux at these interfaces. For this purpose, continuity of heat flux principle is applied to determine the thermal conditions on the cylindrical mesh points at each of the solid-fluid interfaces whereas interpolation relations, representing the principle of continuity of temperature, are applied to calculate the temperature on the bipolar mesh points at each of the interfaces. At the interface points, continuity of temperature and continuity of heat flux can be expressed in finite-difference forms as follows:

At the corner points I through IV, shown in Fig. 1(d), continuity of temperature and heat flux are expressed by the following relations, in which b, n, c and s are numerical indices replacing the index i at these corners; the first pair (b and n) in the fluid zone and the second pair (c and s) in the solid zone, respectively.

At $\xi = 0$ (Widest Gap, $j$=1) *[Points I (on outer interface) and II (on inner interface)]*

$$\theta_f(b+1,1)=\theta_s(s+1,1),$$
$$KR*H(b+1,1)\left[\frac{\theta_s(c+1,1)-\theta_s(c,1)}{\Delta R}\right]=\frac{\theta_f(n+1,1)-\theta_f(n,1)}{\Delta\eta} \quad (17)$$

At $\xi=\pi$ (Narrowest Gap, $j=M+1$) *[Points III (on inner interface) and IV (on outer interface)]*

$$\theta_f(b+1,M+1)=\theta_s(s+1,M+1),$$
$$KR*H(b+1,M+1)\left[\frac{\theta_s(c+1,M+1)-\theta_s(c,M+1)}{\Delta R}\right]=\frac{\theta_f(n+1,M+1)-\theta_f(n,M+1)}{\Delta\eta} \quad (18)$$

The continuity of temperature and heat flux on rest of the mesh points ($2 \le j \le M$) are expressed using the following relations:

$$\theta_f(b+1,j)=\theta_s(s+1,j),$$
$$\theta_f(b+1,j+1)=\theta_s(s+1,j+1),$$
$$\theta_f(b+1,j-1)=\theta_s(s+1,j-1),$$

$$KR*H(b+1,j)\left[\frac{\theta_s(c+1,j)-\theta_s(c,j)}{\Delta R}+\frac{1}{NR}\frac{\theta_s(s+1,j+1)-\theta_s(s+1,j-1)}{2\Delta\phi}\right]=$$
$$\frac{\theta_f(n+1,j)-\theta_f(n,j)}{\Delta\eta}+\frac{\theta_f(b+1,j+1)-\theta_f(b+1,j-1)}{2\Delta\xi} \quad (19)$$

where, $2 \le j \le M$

In equations (17 through 19):

$\theta_s = \theta_{so}$ (For Outer Interface), $\theta_s = \theta_{si}$ (For Inner Interface)

$\Delta R = \Delta R_o$ (For Outer Interface), $\Delta R = \Delta R_i$ (For Inner Interface)

$NR = NR_3$ (For Outer Interface), $NR = NR_2$ (For Inner Interface)

*The values of the numerical indices b, c, n and s are*

$b = 0$ (For Outer Interface), $b = N$ (For Inner Interface)

$c = NSO$ (For Outer Interface), $c = 1$ (For Inner Interface)

$n = 1$ (For Outer Interface), $n = N$ (For Inner Interface)

$s = NSO$ (For Outer Interface), $s = 0$ (For Inner Interface)

**Interpolation of Temperature on Interfaces:**

At both interfaces, interpolation relations are used to evaluate the temperature at every mesh point of the bipolar grid by means of the temperatures at the two neighboring mesh points of the cylindrical grid. The *x*-coordinate of the grid points is used for this purpose. This interpolation can be expressed as follows (See Fig. 1(d)):

***Fluid temperatures on the outer interface:***

$$\theta_f(1,j)=\theta_{so}(NSO+1,jj)+\left[\theta_{so}(NSO+1,jj+1)-\theta_{so}(NSO+1,jj)\right]\left[\frac{X_f(1,j)-X_{so}(1,jj)}{X_{so}(1,jj+1)-X_{so}(1,jj)}\right] \qquad (20)$$

***Fluid temperatures on the inner interface:***

$$\theta_f(N+1,j)=\theta_{si}(1,jj)+\left[\theta_{si}(1,jj+)-\theta_{si}(1,jj)\right]\left[\frac{X_f(N+1,j)-X_{si}(1,jj)}{X_{si}(1,jj+1)-X_{si}(1,jj)}\right] \qquad (21)$$

**Method of Solution**

In practice, the dimensions of the channel ($l$ *and* $D_h$) and both the wall conditions and ambient temperature are normally known while the volumetric flow rate $f$ (and hence $F$) is unknown. However, the present model and method of solution are handling the problem in a reverse manner, i.e. obtaining an unknown dimensionless channel height ($L$) for a given dimensionless volumetric flow rate ($F$). Therefore, the condition $P$=0 at $Z$=$L$ is not explicitly imposed on the solution, but continually checked for satisfaction; recall that the governing equations (4-9) are parabolic in $Z$ and need only one condition with respect to $Z$. Due to symmetry, these equations need to be solved in only half the domain, i.e. for $0 \le \xi \le \pi$. The problem under investigation is governed by six dimensionless parameters, namely, the radius ratio ($NR_2$), the eccentricity ($E$), the Prandtl number ($Pr$), inlet fluid velocity ($U_o$), conductivity ratio ($KR$) and thicknesses of the two walls (*Owall* and *Iwall*).

For a fluid of a given $Pr$ in an annulus of given $NR_2$ and $E$, the solution starts by computing the corresponding values of $\eta_i$ and $\eta_o$ by means of the relations given in the nomenclature. Selecting the numbers of increments in $\eta$ and $\xi$ directions ($N$ and $M$, respectively) the values of $\Delta\eta$ & $\Delta\xi$ can be computed by using the relations given in the nomenclature. Similarly, for the solid walls, by selecting the values of $NR_1$ and $NR_4$ and the number of radial increments in the outer and inner walls and the number of increments in the tangential ($\phi$) direction (*NSO, NSI* and $M$, respectively), the values of $\Delta R_o$, $\Delta R_i$ and $\Delta\phi$ can be determined. Assume a value for the uniform axial velocity at the entrance $U_o$ (i.e., F since $F=U_o(1-NR_2^2)$). Since at entrance $W = V = 0$, the inlet pressure will be $P_o = -\frac{U_o^{\,2}}{2}$.

For each axial location (cross-section), the energy equations for the fluid (13) and solids (14 and 15) are simultaneously solved for the temperatures using Gauss-Seidel iteration. The solution starts by simultaneously solving Eqs. (13), (14) & (15), using Gauss-Seidel iteration, to obtain the unknown values of $\theta_f$, $\theta_{si}$ and $\theta_{so}$ at the second cross-section. Within the Gauss-Seidel iteration process, the temperature values of the cylindrical grid points at the two interfaces are calculated using the principles of continuity of temperature and continuity of heat flux. The temperature values of the bipolar grid points at both the interfaces are computed by interpolating between the temperature values of the two neighboring cylindrical grid points at both sides of each bipolar grid point. To solve for the two unknowns $P$ and $U$ at the aforesaid plane, the integral form of the continuity equation (16) and the finite difference form of the axial momentum equation (11) are used. The resulting set of algebraic equations is solved by a modified Gauss-Jordan elimination scheme. Then, $\xi$-Momentum equation (12) is solved for $W$-velocity component using Gauss-Seidel iteration method. Finally, the continuity equation (10) is used to evaluate $V$-velocity component at all the interior grid points. These steps are repeated to advance axially (vertically) until the pressure defect ($P$) becomes zero indicating that channel exit has been reached.

**Results and Discussion**

The Grashof number is inherent in the dimensionless formulation of the problem ($Gr* = \frac{GrD_h}{l}$) and thus it is not explicitly needed for the solution. However, six other similarity parameters are explicitly required to solve the problem under consideration. These are the fluid annulus radius ratio ($NR_2$), the dimensionless eccentricity ($E$), the dimensionless flow rate $F$ (or effectively $U_o=F/(1-NR_2^2)$), solid-fluid thermal conductivity ratio ($KR$), inner and outer cylinder walls thickness (*Iwall* and *Owall*) and the Parandtl number ($Pr$). However, one should recall that the inlet velocity ($U_o$) and hence the inlet pressure ($P_o$) and the volumetric flow rate ($F$) are not predetermined initial conditions independent of the channel height as in the case of forced flows. Rather, each of them is dependent on the channel height ($L$) and the applied thermal boundary conditions on the annulus walls. The numerical solutions in this paper are obtained for a fluid of $Pr$=0.7 in an annulus of radius ratio, $NR_2$=0.5 and dimensionless eccentricity, $E$=0.5.

Computational errors can be minimized by increasing the number of grid points or in other words, decreasing the mesh size. To establish grid independence, twelve different mesh sizes for fluid annulus and inner & outer solid walls were tested. Among all, the mesh sizes of 25 x 25 (in $\eta$ and $\xi$ directions), 20 x 25 (in $r$ and $\phi$ directions) and 10 x 25 (in $r$ and $\phi$ directions) for the

fluid annulus, outer cylinder wall and inner cylinder wall, respectively were selected representing the best compromise between the execution time of the program and percentage difference in the obtained results (less than 1 %). To clarify quantitatively this point, Table 1 shows examples of the results obtained using some of the tested mesh-size combinations in the fluid annulus. This table gives comparisons between the values at the exit cross section for the inner wall heat flux, the outer wall heat flux, the inner wall Nusselt number, the outer wall Nusselt number, and the mixing-cup temperature. Moreover, it gives also the computer time needed for each tested mesh combination. The results in this table are compared with reference to the corresponding results pertaining to the 30x 30-mesh (in $\eta$ and $\xi$ directions). The results in the table show that the mesh of 25 x 25 (in $\eta$ and $\xi$ directions) gives results within less than 1% of those corresponding to the 30x 30-mesh.

To check the adequacy of the present computer code, special runs were carried out simulating the three different limiting cases of conventional (without conjugation) forced convection, conjugate forced convection and conventional natural convection in the given eccentric annuli. For both conventional forced and natural convection cases, the present computer code was made to run for very large values of solid-fluid thermal conductivity ratio (*KR*=1000) and very thin cylinder walls (*Iwall*=0.001 and *Owall*=0.002), such that the conjugate effect would be negligible. On the other hand, the present computer code can simulate forced convection cases when the values of the inlet velocity $U_o$ exceed the corresponding limiting values for natural convection [19]. The results of these special computer code experimentations are as follows.

First, special runs of the present computer code were made to compare the results obtained for fully-developed conventional (without conjugation) forced convection in eccentric annuli with that reported by Trombetta [10], El-Shaarawi and Haider [17], and Shah and London [20]. The maximum deviations between the obtained results and those of Trombetta [10], El-Shaarawi and Haider [17], and Shah and London [20] were about 0.35 %, 0.12 % and 1.34 %, respectively, as shown in Table 2. The present computer code was also validated with conventional forced convection results obtained by El-Shaarawi et. al. [14] for fully developed values of mixed mean temperature ($\theta_{m,fd}$); the maximum percentage difference was found to be 0.032 %.

Secondly, the present computer code was validated for conjugate forced convection case in eccentric annuli by comparing the results obtained from a pertaining run of the present code for both the developing and fully developed temperature profiles across the widest gap ($\Psi$=0) of the eccentric annulus and the corresponding results of El-Shaarawi and Haider [17]; excellent

agreement of the results can be observed as the maximum deviation between the obtained results and those of [17] never exceeded 0.23 %.

Thirdly, a special computer run simulating conventional natural convection was done. The obtained results for the channel height required to suck specific flow rates under thermal boundary conditions of first kind are compared in Fig. 2 with the corresponding results of [16].

The selected values of inner and outer wall thicknesses are taken from the standard practical values shown in Table 3. The values of solid-fluid conductivity ratio (*KR*) are selected in such a way to represent all of its practical values shown in Table 4. Owing to space limitations, only a representative sample of the results will be presented. Figures 3(a) and 3(b) present the important variation of induced flow rate versus the channel height for different values of conductivity ratio for cases (I) and (O), respectively. In both cases, as the channel height increases the flow rate increases. Looking at Fig. 3(a), one can observe two different trends of flow rate variation with increasing solid-fluid conductivity ratio (*KR*). For short channels, the flow rate is high for large values of *KR* whereas this behavior reverses for correspondingly high channels. Small conductivity ratio means that the solid walls of the annulus act like thermal insulators. Consequently, the inner heated wall resists the heat flow into the fluid, which decreases the temperature level at the inner solid-fluid interface. On the other hand, the outer cooled wall with small conductivity ratio acts as an insulator preventing the heat to flow out from the fluid to the surrounding, which results in raising the temperature at the outer solid-fluid interface. These two opposing effects will interchange their places from the inner to the outer interface for case (O).

For case (I), when the channel height is small and solid-fluid conductivity ratio (*KR*) increases, the temperature on the inner solid-fluid interface increases. Meanwhile, the outer wall effect is not prominent in this case because the heat signal is not fully sensed by the outer interface due to short channel height. This results in the increased flow rate into the channel. For high channels, the situation reverses because the outer wall cooling effect dominates due to its larger surface area at high solid-fluid conductivity ratio enabling more heat to flow through the outer wall. The result is the decrease in temperature on outer solid-fluid interface. This reduces the induced flow rate into the channel. For case (O), the effect of increasing solid-fluid conductivity ratio on induced flow rate remains consistent for all the channel height range, i.e. having increased flow rate with increasing values of conductivity ratio as shown in Fig. 3(b). In this case the outer wall heating effect is dominant on the cooling effect of the inner wall throughout the channel height. The effect of increased flow rate enables the fluid to absorb more heat, which increases the buoyancy force inducing more flow into the channel.

Examples of the temperature variation with conductivity ratio along the line of symmetry are shown for case (I) at the widest and the narrowest gaps of the annulus in Figs. 4(a) and 4(b), respectively. Figures 5(a) and 5(b) show the variations of the total heat absorbed ($\overline{Q}$) by the fluid versus channel height ($L=1/Gr^*$) for different values of solid-fluid conductivity ratio for cases (I) and (O), respectively. Both Figs. 5(a) and 5(b) show similar trend as was observed in Figs. 3(a) and 3(b). This is due to the fact that the total heat absorbed ($\overline{Q}$) equals the product of induced flow rate ($F$) and the mean bulk temperature at channel exit ($\theta_{m,ex}$). This makes the variation of the total heat absorbed ($\overline{Q}$) with conductivity ratio directly linked with the induced flow rate ($F$).

Figure 6(a) shows the effect of the wall thickness on the variation of flow rate with channel height for case (I). For short channels, the induced flow rate decreases as the wall thicknesses increase. This behavior reverses for considerably high channels. Thick walls have the same opposing effect as that for walls with small conductivity ratio, i.e. inner wall resisting the heat to flow into the fluid while outer wall preventing the heat to flow out of the fluid. For case (I), when the channel height is small, thick walls show lower temperature values on inner solid-fluid interface than for thin walls. This enables less heat to be absorbed by the fluid resulting in small buoyancy forces. The outer wall effect is not prominent in such short channels. Both these effects result in the decrease in the flow rate into the channel as shown in Fig. 6(a). For higher channels, the situation reverses for thick walls because now there is sufficient height of the channel for the heat to be absorbed by the fluid along with the dominance of the outer wall effect resisting more the heat to flow through it. This results is an increase in the temperature on outer solid-fluid interface along with the higher temperature level in the fluid, hence increasing the induced flow rate into the channel. One can also say that the cooling effect of the outer wall is suppressed in the channel having thick walls. For case (O), the effect of increasing the wall thicknesses on induced flow rate remains consistent for all channel heights range, i.e. having reduced flow rate for thick walls as can be seen in Fig. 6(b). In this case, the amount of heat entering the fluid annulus from outer cylinder wall decreases when the wall thickness is increased. This imposes an overall effect of reducing the heat gained by the fluid, therefore, decreasing the induced flow rate.

To help in explaining the phenomenon, representative results of temperature profile across the channel are shown in Fig. 7(a) and 7(b) for a specific flow rate of 0.00825 at an axial (vertical) location of $1.59\text{x}10^{-2}$ in case (I) for thin and thick walls, respectively. In each of these two figures, the temperature profiles are shown for $\Psi = 0$ (widest gap) & 1 (narrowest gap) and help in explaining the phenomenon. Very thin walls show almost zero temperature gradient as

can be seen in Fig. 7(a) whereas the temperature gradient increases in thick walls (Fig.7(b)) leading to a decrease in temperature on the inner solid-fluid interface and an increase in temperature on the outer interface.

Figures 8(a) and 8(b) show the effect of the wall thicknesses on the total heat absorbed ($\overline{Q}$) by the fluid versus the channel height for case (I). Recalling that the total heat absorbed ($\overline{Q}$) is directly linked to the induced flow rate ($F$) as explained earlier, it follows that the trend of $\overline{Q}$ is generally similar to that observed in Figs. 6(a) and 6(b). Rather than using Nusselt number on the walls of the annulus, the total heat absorbed ($\overline{Q}$) can be used to directly obtain the heat gained by the fluid from entrance up to the annulus exit. As can be seen from Figs. 8(a) and 8(b), values of $\overline{Q}$ in case (O) are larger than the corresponding values in case (I), provided all other parameters are the same. This is a result of the larger heating surface area in case (O) than in case (I).

Figure 9 shows the effect of KR on the percentage difference between the two values of the induced free convection flow rates corresponding to the cases with and without conjugation for various channel heights for case (I). The figure shows that, for a given channel height, increasing the conductivity ratio reduces the conjugate effect and brings the induced fluid flow rate in the channel closer to that of the conventional case (reduction in percent difference in $F$ from conventional case as a result of increasing the conductivity ratio ($KR$)). On the other hand, Fig. 9 shows that increasing the channel height, for a given conductivity ratio ($KR$), results in an increase in percent difference in the flow rate from the conventional case. This means that conjugate effect is more pronounced in high channels than that in short channels.

It is of practical importance to know the values of the conductivity ratio beyond which the conjugate effect can be neglected. These values are termed as the critical values. The critical values of conductivity ratio, for given eccentricity ($E$) and radius ratio ($NR_2$), has been arbitrarily defined as the values which cause the channel height to differ by no more than 2% from the conventional (without conjugation) solution results. Based on a similar arbitrary definition for the critical conductivity ratio, El-Shaarawi and Haider [17] obtained a unique value for the critical conductivity ratio for the conjugate heat transfer in the forced convection regime. The present case of conjugate heat transfer in the free convection regime has no single value for the critical conductivity ratio. Unlike the conjugate heat transfer in the forced convection regime, the critical conductivity ratio in the present case is a function of the channel height ($L$), as can be seen in Fig. 9. Figure 10 gives the critical conductivity ratio against the channel height (i.e.,

Grashof number) for the annulus under consideration ($NR_2$=0.5, $E$=0.5, *Iwall*=0.1, *Owall*=0.2, $Pr$=0.7) for case (I). The critical conductivity ratio ($KR_{cr}$) increases with the channel height.

## Conclusions

Combined conduction-laminar free convection heat transfer in vertical eccentric annuli has been numerically investigated. A finite-difference algorithm has been developed to solve the bipolar model equations. Numerical results are presented for a fluid of Prandtl number, $Pr$=0.7 in an annulus of radius ratio, $NR_2$=0.5 and dimensionless eccentricity, $E$=0.5. Practical ranges of the solid fluid conductivity ratio (*KR*=1-1000) and the dimensionless walls thickness that are commonly available in pipe standards (*Iwall*=0.01-0.2 and *Owall*=0.02-0.4) have been investigated. The effect of conjugation on the variations of the induced flow rate ($F$) and the heat absorbed by the fluid within the channel height has been investigated for two sets of boundary conditions (*Cases I and O*).

Results show that increasing the thermal resistance of the walls, i.e., decreasing the solid-fluid thermal conductivity ratio or increasing the cylinder walls thickness may cause an increase in the induced flow rate ($F$) for short annuli in case (I) whereas it always causes a decrease in case (O). Similar trend is observed for total heat absorbed ($\overline{Q}$) by the fluid in the eccentric annulus. Increasing the thermal resistance of the walls makes the conjugate effect tangible. Also the obtained results show that the conjugation effect is more pronounced for case (O) than case (I). Finally, the critical values of conductivity ratio for a range of channel heights ($L$) above which the conjugate effect can be neglected have been determined for use in practical applications.

## REFERENCES

1. Anand, N. K. and Tree, D. R., “Some studies of the effects of axial conduction in a tube wall on the steady-state laminar convective heat transfer”, *Journal of Heat Transfer*, Vol. 109, pp. 1025-1028 (1987).

2. Kim, S. H. and Anand, N. K., “Effect of wall conduction on free convection between asymmetric heated vertical plates: uniform wall heat flux”, *International Journal of Heat and Mass Transfer*, Vol. 33, No. 5, pp. 1013-1023 (1990).

3. Kim, S. H., Anand, N. K. and Fletcher, L. S., “Free convection between series of vertical parallel plates with embedded line heat source ”, *Journal of Heat Transfer*, Vol. 113, pp. 108-115 (1991).

4. Sakakibara, M., Mori, S. and Tanimoto, A., "Conjugate heat transfer laminar flow in an annulus", *The Canadian journal of chemical engineering*, Vol. 65, pp. 541-549 (1987).

5. El-Shaarawi, M.A.I., Al-Nimr, M.A. and Hader, M.A., "Transient conjugated heat transfer in concentric annuli", *International journal of numerical methods in heat and fluid flow*, Vol. 5, pp. 459-473 (1995).

6. El-Shaarawi, M.A.I. and Negm, A. A. A., "Transient combined natural convection-conduction in open-ended vertical concentric annuli", *Heat and mass transfer*, Vol. 35, pp. 133-141 (1999).

7. Shu, C. and Wu, Y.L., "Domain-free discretization method for doubly connected domain and its application to simulate natural convection in eccentric annuli", *Computer Methods in Applied Mechanics and Engineering*, Vol. 191, No. 17-18, p. 1827-1841 (2002).

8. Redberger, P.J. and Charles, M.E., "Axial laminar flow in a circular pipe containing a fixed eccentric core", *The Canadian journal of Chemical Engineering*, Vol. 40, pp. 148-151 (1962).

9. Cheng, K.C. and Hwang, G.J., "Laminar forced convection in eccentric annuli", *A. I. Ch. E. Journal*, Vol. 14, No. 3, pp. 510-512 (1968).

10. Trombetta, M.L., "Laminar forced convection in eccentric annuli", *International Journal of Heat and Mass Transfer*, Vol. 14, pp. 1161-1172 (1972).

11. Manglik, R.M. and Fang, P.P., "Effect of eccentricity and thermal boundary conditions on laminar fully developed flow in annular ducts", *International journal of heat and fluid flow*, Vol. 16, pp. 298-306 (1995).

12. Feldman, E.E., Hornbeck, R.W. and Osterle, J. F., "A numerical solution of laminar developing flow in eccentric annular ducts", *International journal of heat and mass transfer*, Vol. 25, No. 2, pp. 231-241 (1982).

13. Feldman, E.E., Hornbeck, R.W. and Osterle, J. F., "A numerical solution of temperature for laminar developing flow in eccentric annular ducts", *International journal of heat and mass transfer*, Vol. 25, No. 2, pp. 243-253 (1982).

14. El-Shaarawi, M.A.I., Abualhamayel, H. I. and Mokheimer, E.M.A., "Developing laminar forced convection in eccentric annuli", *Heat and mass transfer*, Vol. 33, pp. 353-362 (1998).

15. El-Shaarawi, M.A.I., Mokheimer, E. M. A., "Free convection in vertical eccentric annuli with a uniformly heated boundary", *International Journal of Numerical Methods for Heat & Fluid flow*, Vol. 8, No. 5, pp. 488-503 (1998).

16. El-Shaarawi, M.A.I., Mokheimer, E. M.A., "Developing free convection in open ended vertical eccentric annuli with isothermal boundaries", *Journal of Heat Transfer, Transaction ASME*, Vol. 121, No. 1, pp. 63-72 (1999).

17. El-Shaarawi, M.A.I. and Haider, S. A., "Critical conductivity ratio for conjugate heat transfer in eccentric annuli", *International Journal of Numerical Methods for Heat and Fluid Flow*, Vol. 11, No. 2, pp. 255-277 (2001).

18. Hughes, W.F. and Gaylord, E.W., Basic equations of Engineering Science, Schaum Outline series, pp. 150-151 (1964).

19. El-Shaarawi, M. A. I., Mokheimer, E.M.A. and Abulhamayal, H. I., "Limiting values for free convection induced flow rates in vertical eccentric annuli", *Numerical Heat Transfer*, 39A, Vol. 6, pp. 611-630 (2001).

20. Shah, R.K. and London, A.L., *Laminar flow forced convection in ducts,* Academic Press, New York (1978).

## Figure Captions

Fig. 1(a) The geometry and grid points, $NR_2$=0.5, E=0.5, NSO=8, NSI=5, N=10, M=50, Iwall=0.05, Owall=0.1

Fig. 1(b) The domain of solution

Fig. 1(c) Bi-polar coordinate system

Fig. 1(d) Details of the grid points, $NR_2$=0.5, E=0.5, NSO=10, NSI=5, N=15, M=25, Iwall=0.05, Owall=0.1

Fig. 2 Comparison of volumetric flow rate versus channel height with the corresponding conventional (without conjugation) results of [16], $NR_2$=0.5, $NR_1$=0.499, $NR_3$=1, $NR_4$=1.002, N=20, M=20, NSI=25, NSO=25, KR=1000

Fig. 3 Variation of F with L for different values of KR, $NR_2$=0.5, E=0.5, Iwall=0.1, Owall=0.2, (a) Case I, (b) Case O

Fig. 4 Temperature profiles at axial location of $4.36 \times 10^{-3}$ for different values of KR, $NR_2$=0.5, E=0.5, Iwall=0.1, Owall=0.2, F=0.0133, (a) Case I, (b) Case O

Fig. 5 Conjugation effect on the total heat absorbed versus the channel height, $NR_2$=0.5, E=0.5, Iwall=0.1, Owall=0.2, (a) Case I, (b) Case O

Fig. 6 Effect of wall thickness on F-L variation, $NR_2$=0.5, E=0.5, KR=2, (a) Case I, (b) Case O

Fig. 7 Effect of wall thickness on the temperature profiles at $Z=1.59 \times 10^{-2}$, $NR_2$=0.5, E=0.5, KR=2, Owall=0.2, (a) Case I with Iwall=0.01, Owall=0.02, (b) Case O with Iwall=0.2, Owall=0.4

Fig. 8 Effect of wall thickness on $\overline{Q}$ -L variation, $NR_2$=0.5, E=0.5, KR=2, (a) Case I, (b) Case O

Fig. 9 Effect of dimensionless channel height on conjugation effect, $NR_2$=0.5, E=0.5, Iwall=0.1, Owall=0.2

Fig. 10 Critical conductivity ratio versus channel height, $NR_2$=0.5, E=0.5, Iwall=0.1, Owall=0.2

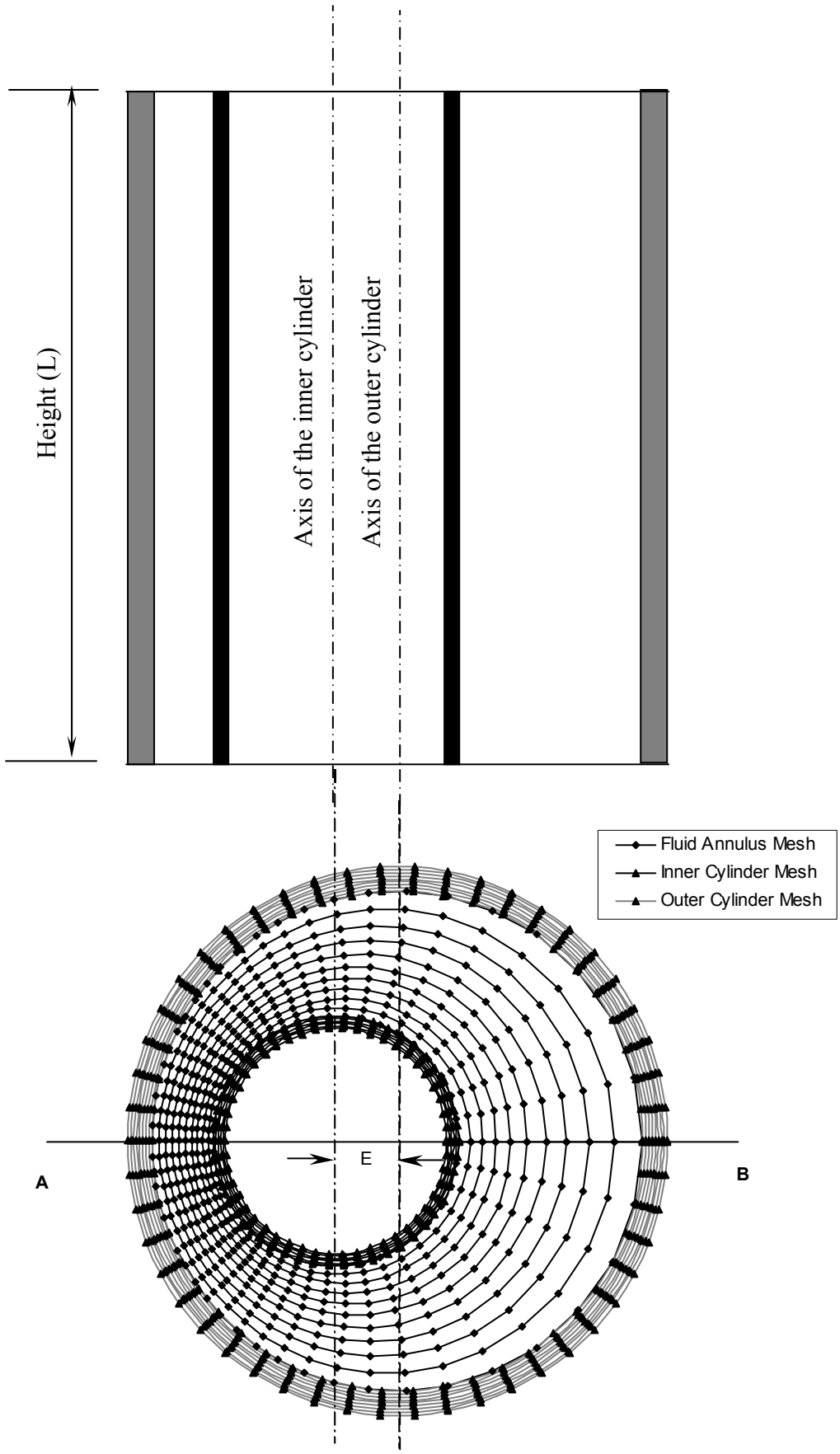
Height (L)
Axis of the inner cylinder
Axis of the outer cylinder
Fluid Annulus Mesh
Inner Cylinder Mesh
Outer Cylinder Mesh
E
A
B

**Fig. 1(a).**

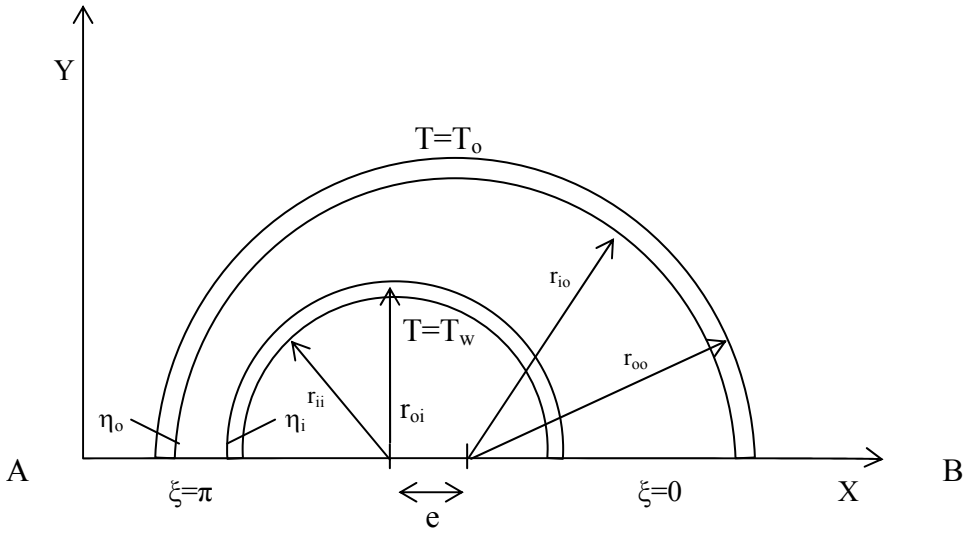
Y
T=T_o
r_io
T=T_w
r_oo
r_ii
r_oi
η_o
η_i
A
ξ=π
e
ξ=0
X
B

**Fig. 1(b).**

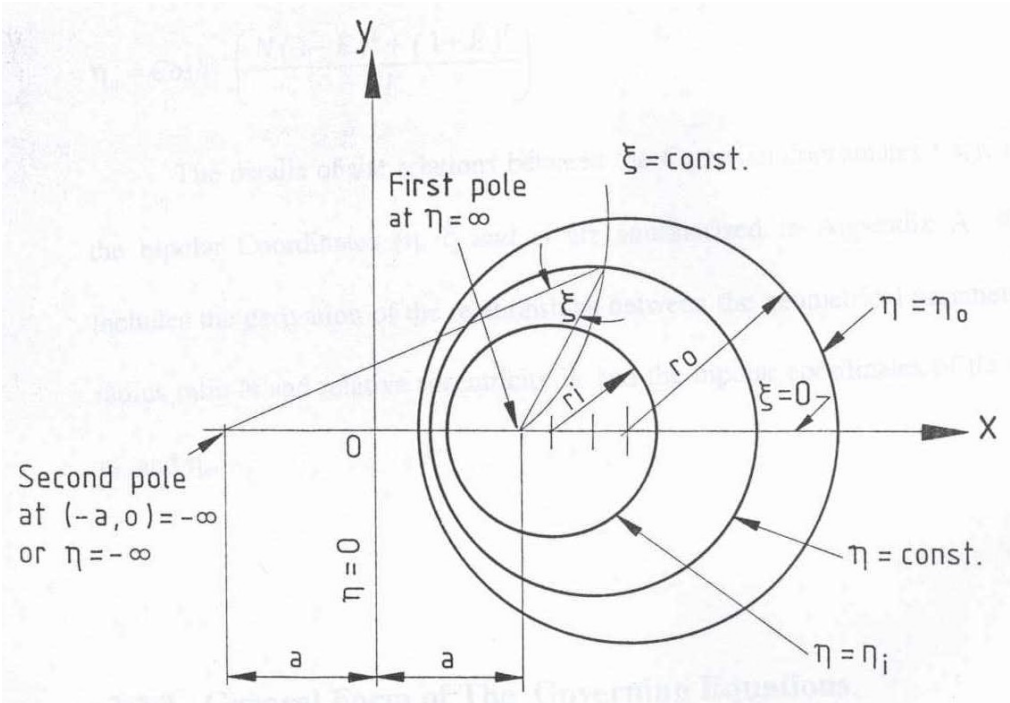
y
ξ = const.
First pole
at η = ∞
ξ
η = η_o
r_o
r_i
ξ=0
X
0
Second pole
at (-a,0) = -∞
or η = -∞
η = 0
η = const.
η = η_i
a
a

**Fig. 1(c).**

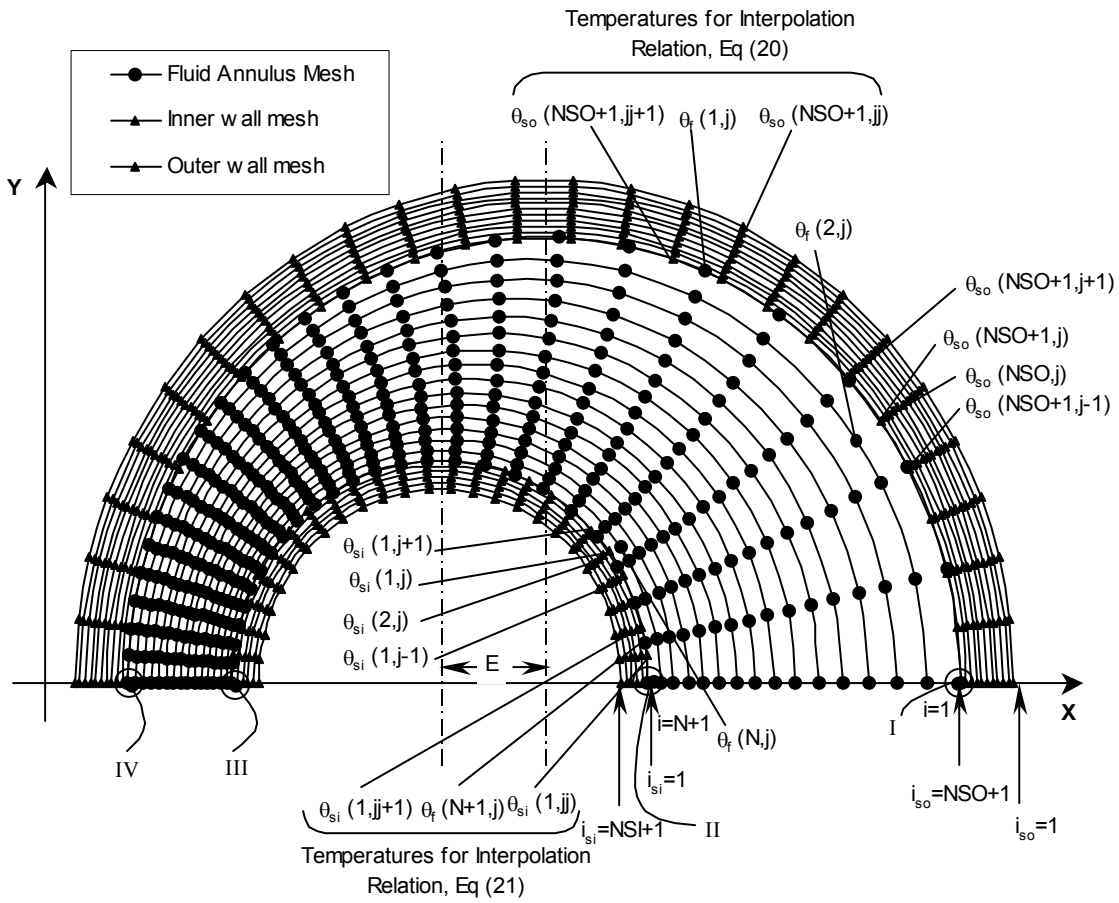
Temperatures for Interpolation
Relation, Eq (20)
Fluid Annulus Mesh
Inner w all mesh
Outer w all mesh
Y
X
θso (NSO+1,jj+1)
θf (1,j)
θso (NSO+1,jj)
θf (2,j)
θso (NSO+1,j+1)
θso (NSO+1,j)
θso (NSO,j)
θso (NSO+1,j-1)
θsi (1,j+1)
θsi (1,j)
θsi (2,j)
θsi (1,j-1)
E
IV
III
I
i=1
i=N+1
θf (N,j)
isi=1
iso=NSO+1
iso=1
θsi (1,jj+1)
θf (N+1,j)
θsi (1,jj)
isi=NSI+1
II
Temperatures for Interpolation
Relation, Eq (21)

**Fig. 1(d).**

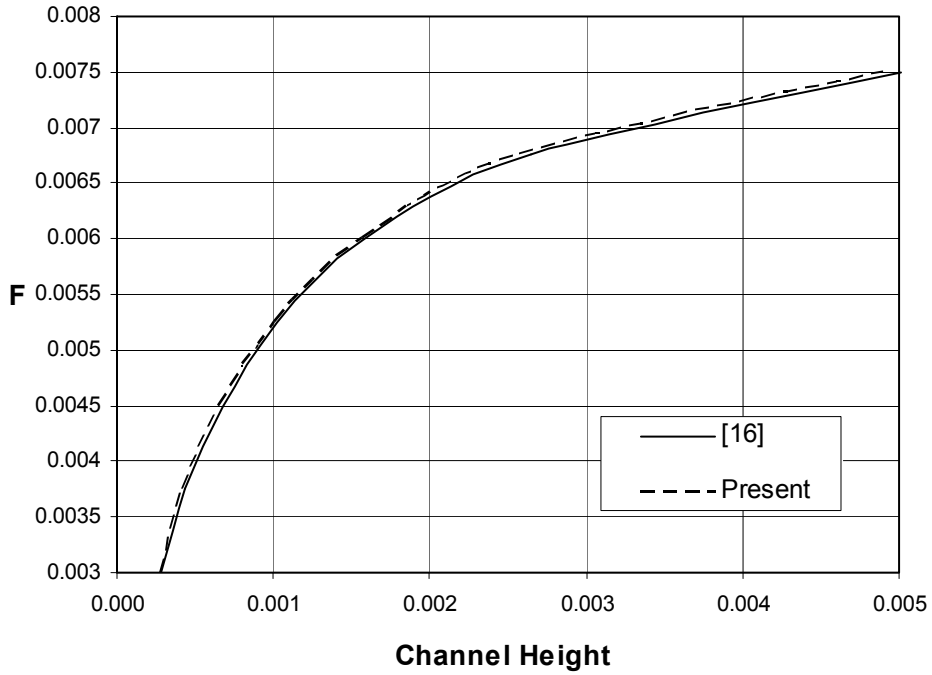


**Fig. 2.**

Case (I)

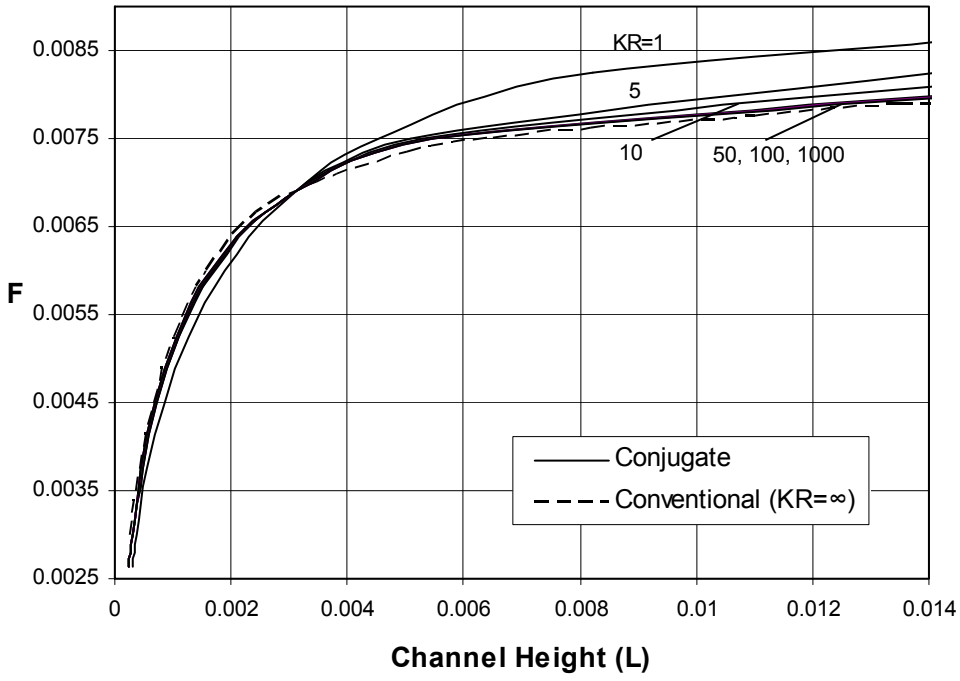


**Fig. 3 (a).**

Case (O)

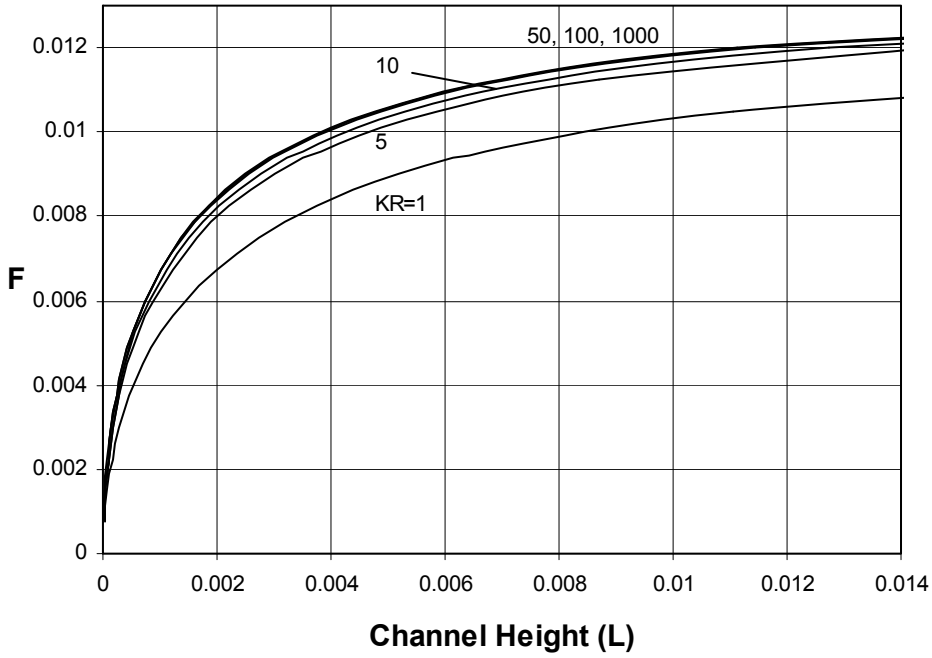


**Fig. 3 (b).**

Case (I)

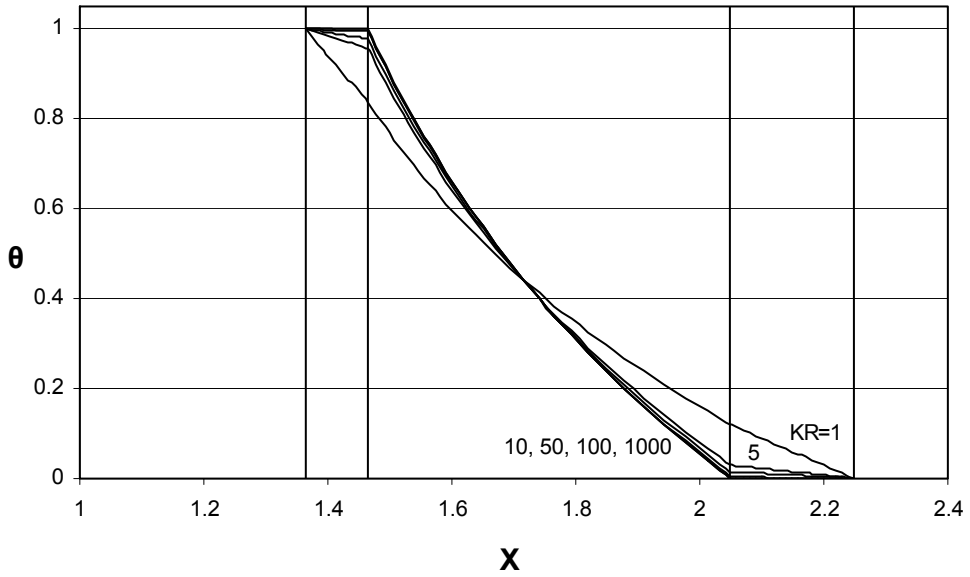


**Fig. 4 (a).**

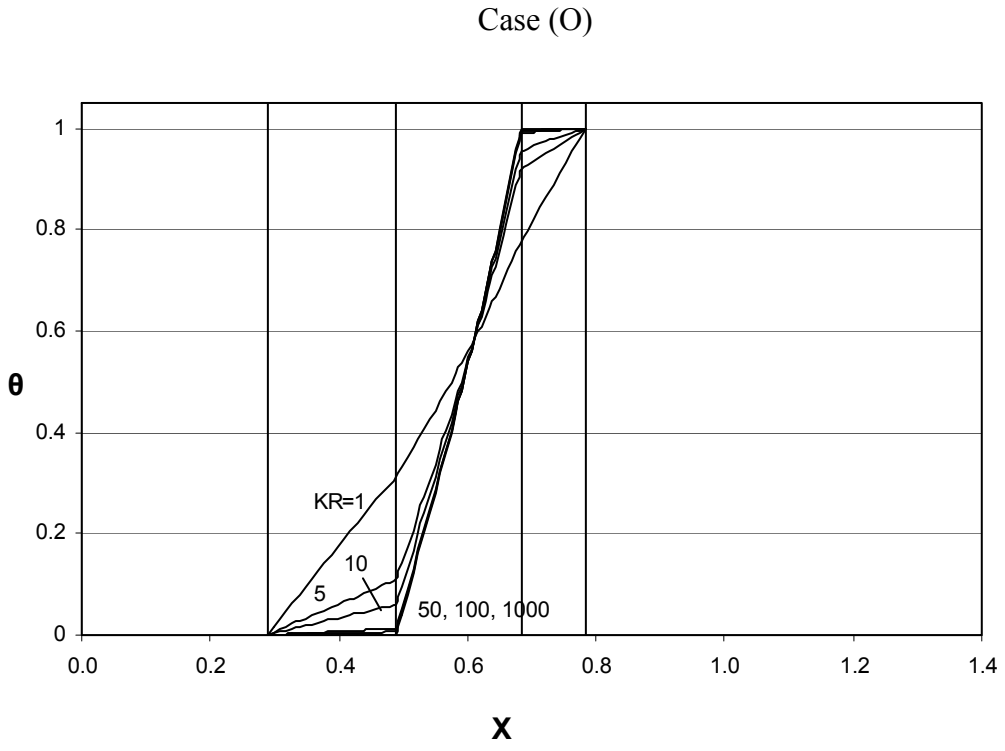
Case (O)
θ
X
KR=1
10
5
50, 100, 1000
0
0.2
0.4
0.6
0.8
1
0.0
0.2
0.4
0.6
0.8
1.0
1.2
1.4

**Fig. 4 (b).**

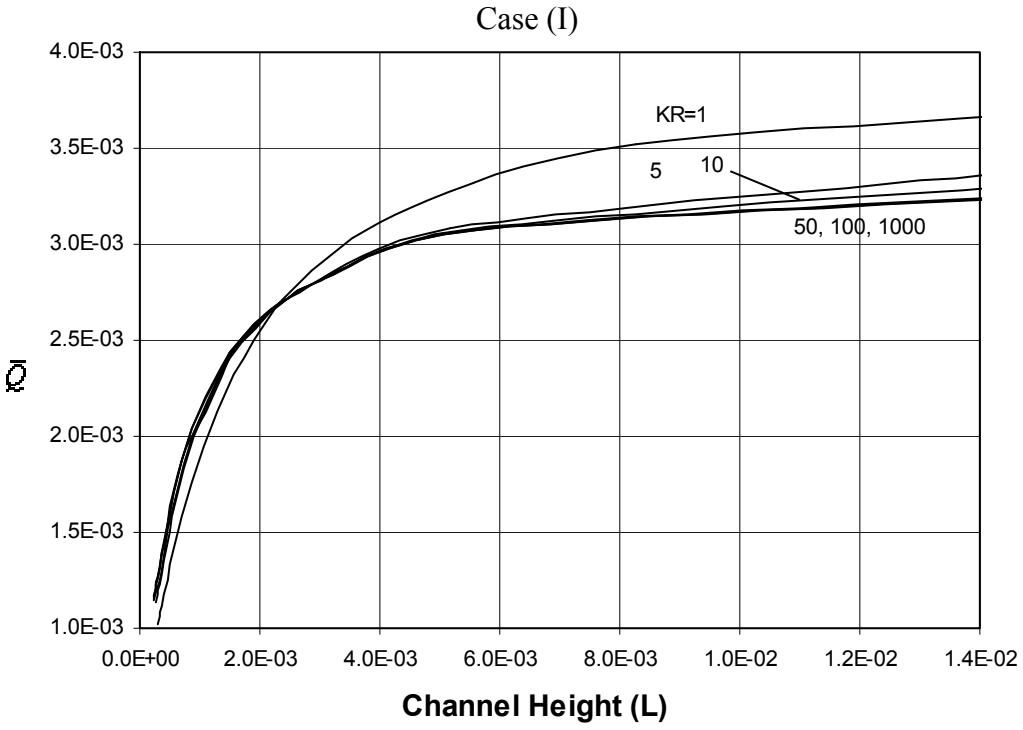
Case (I)
Q̄
Channel Height (L)
KR=1
5
10
50, 100, 1000
1.0E-03
1.5E-03
2.0E-03
2.5E-03
3.0E-03
3.5E-03
4.0E-03
0.0E+00
2.0E-03
4.0E-03
6.0E-03
8.0E-03
1.0E-02
1.2E-02
1.4E-02

**Fig. 5 (a).**

Case (O)

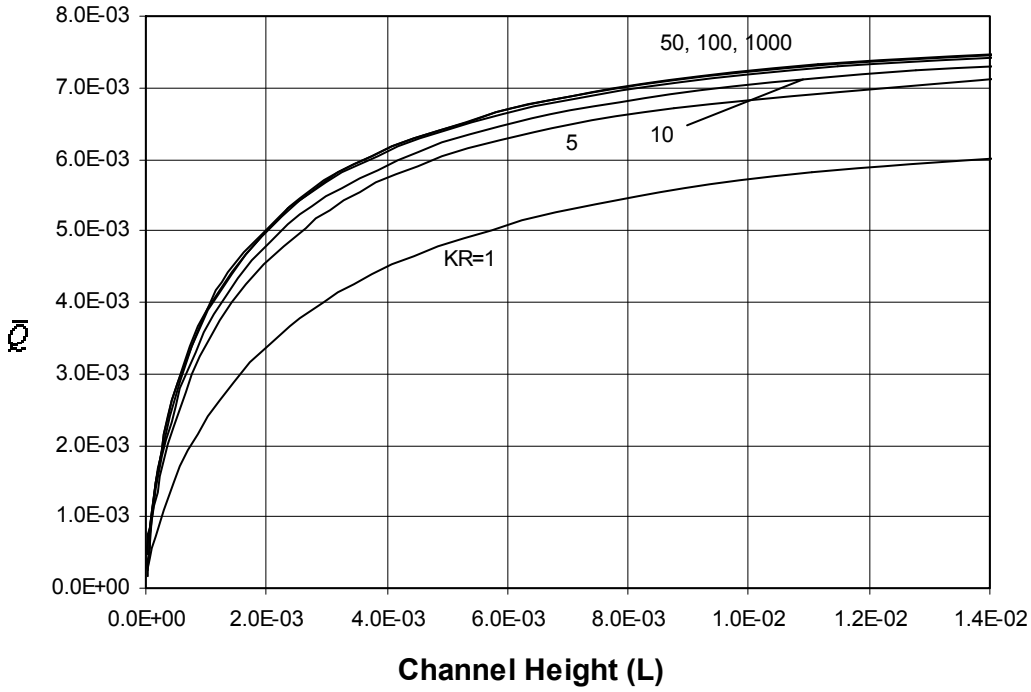


**Fig. 5 (b).**

Case (I)

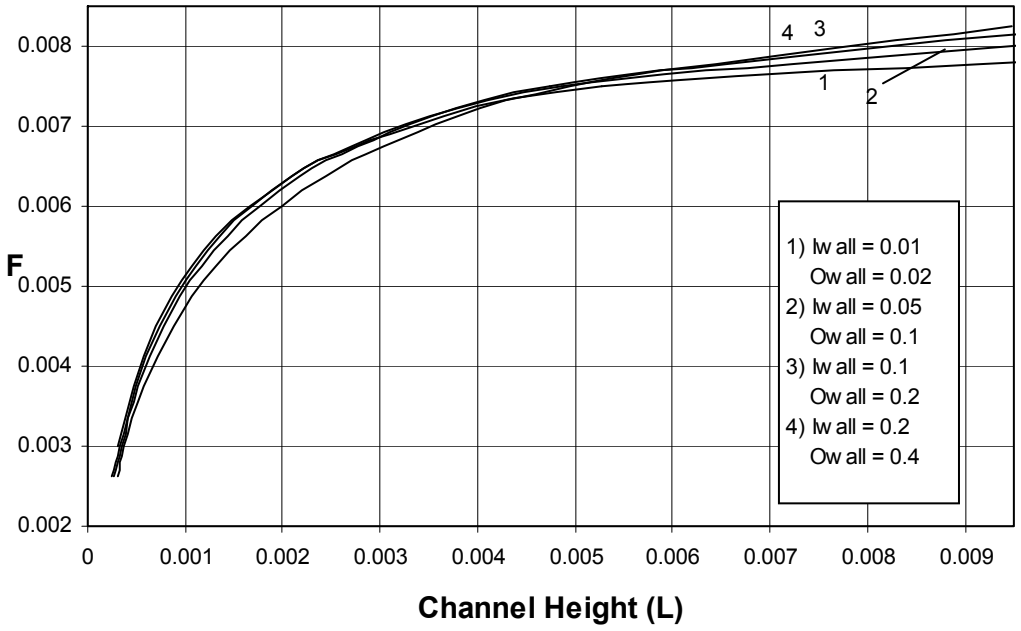


**Fig. 6 (a).**

Case (O)

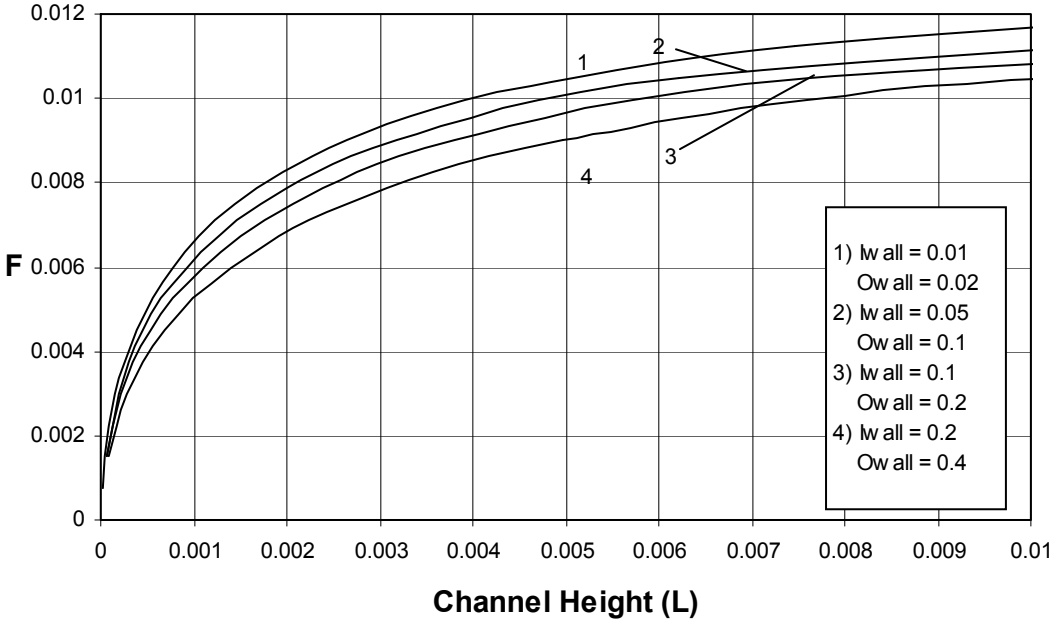


**Fig. 6 (b).**

Case (I)

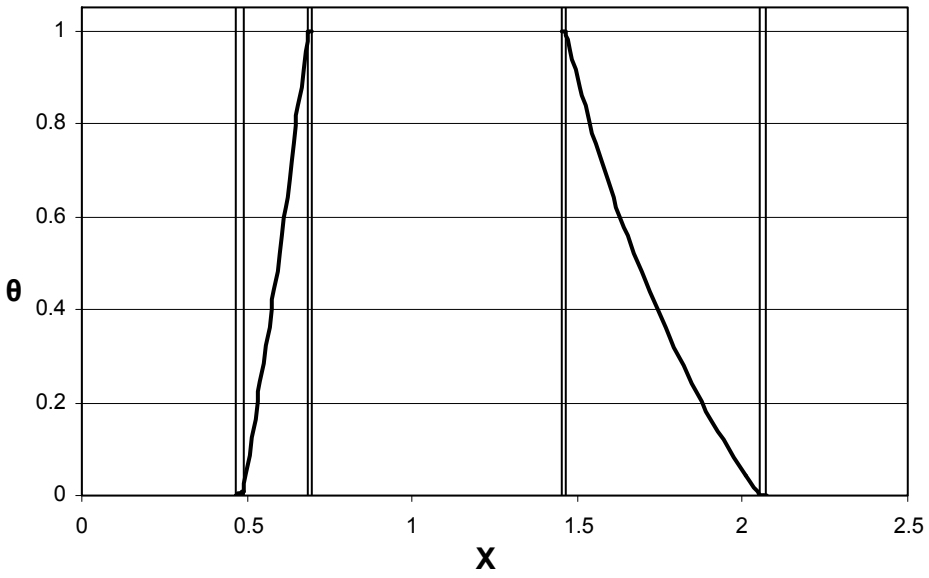


**Fig. 7 (a).**

Case (I)

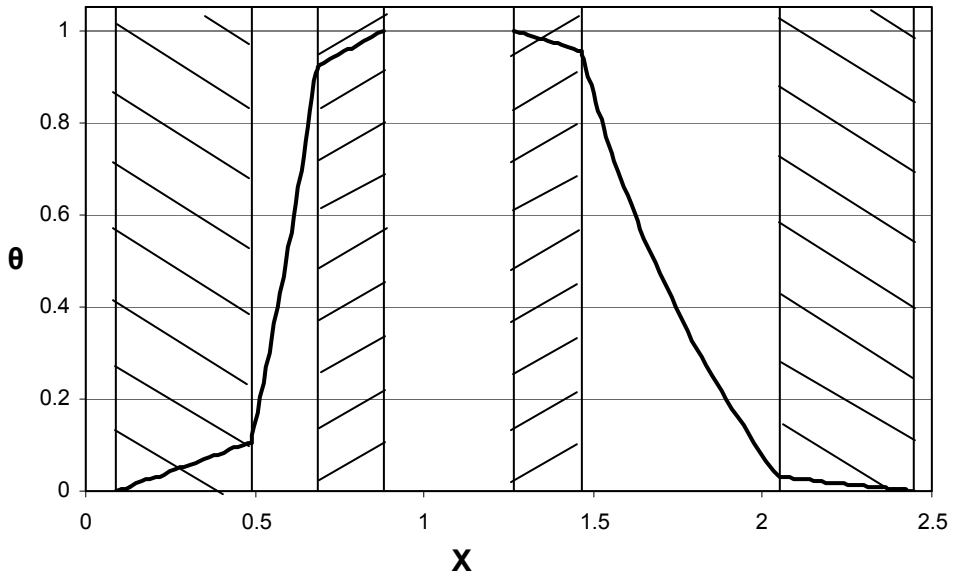


**Fig. 7 (b).**

Case (I)

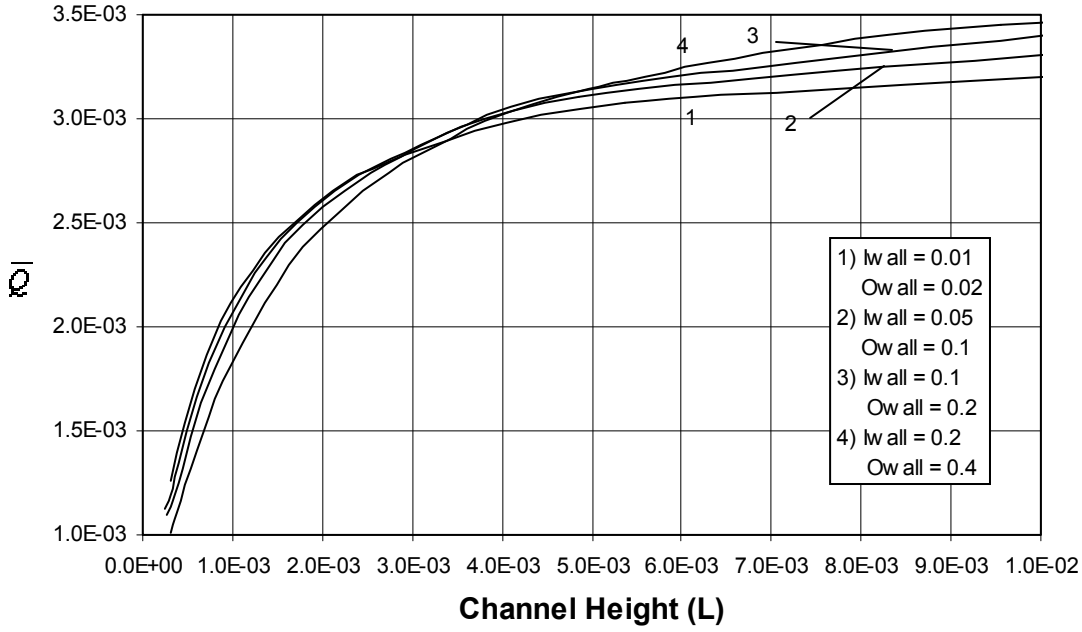


**Fig. 8 (a).**

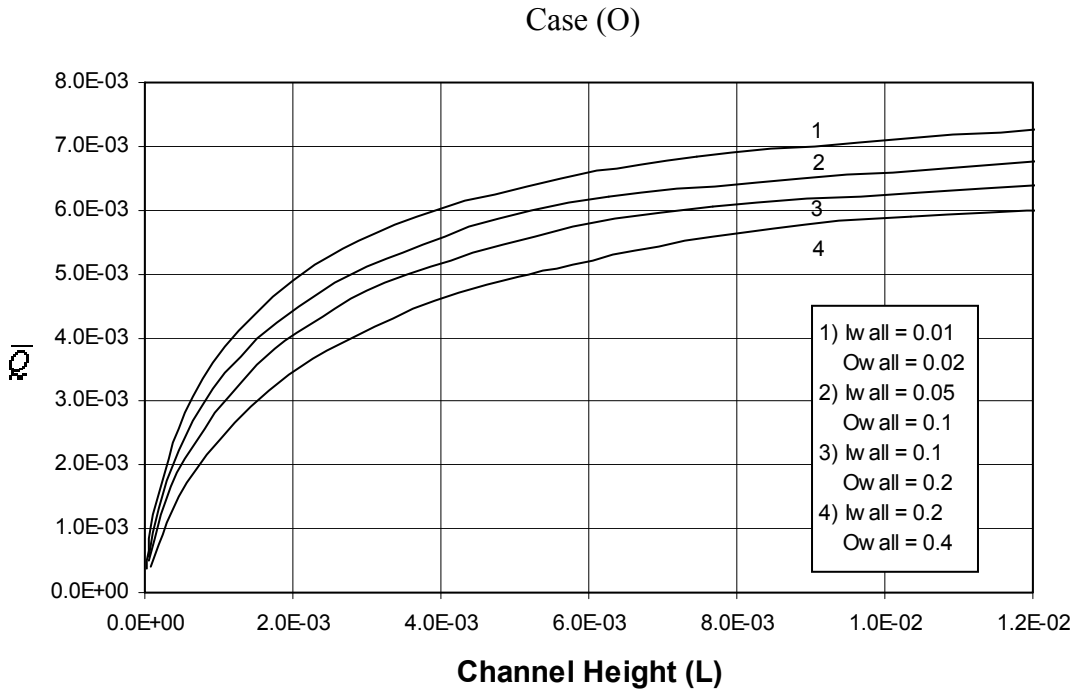
Case (O)
8.0E-03
7.0E-03
6.0E-03
5.0E-03
4.0E-03
3.0E-03
2.0E-03
1.0E-03
0.0E+00
Q
0.0E+00
2.0E-03
4.0E-03
6.0E-03
8.0E-03
1.0E-02
1.2E-02
Channel Height (L)
1
2
3
4
1) Iw all = 0.01
Ow all = 0.02
2) Iw all = 0.05
Ow all = 0.1
3) Iw all = 0.1
Ow all = 0.2
4) Iw all = 0.2
Ow all = 0.4

**Fig. 8 (b).**

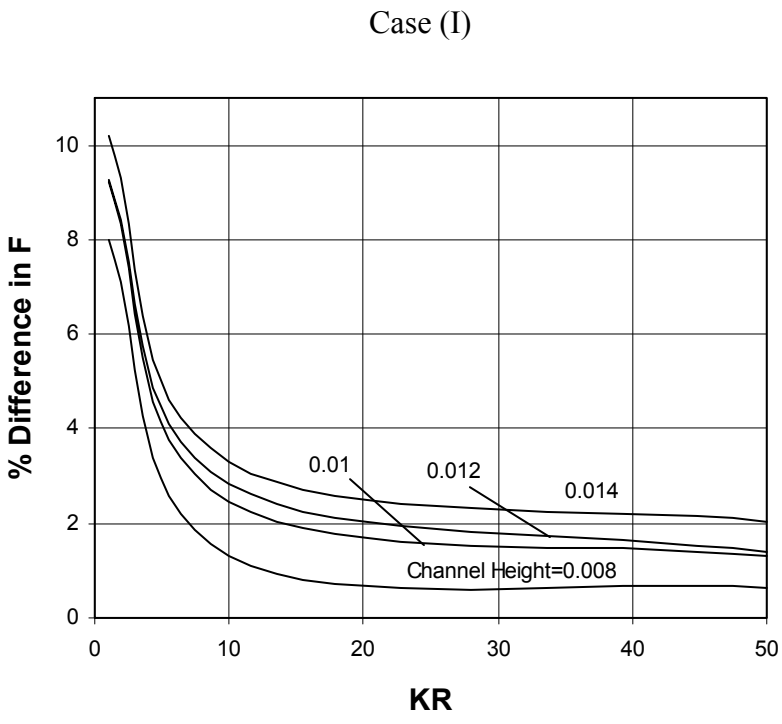
Case (I)
% Difference in F
10
8
6
4
2
0
0
10
20
30
40
50
KR
0.01
0.012
0.014
Channel Height=0.008

**Fig. 9.**

Case (I)

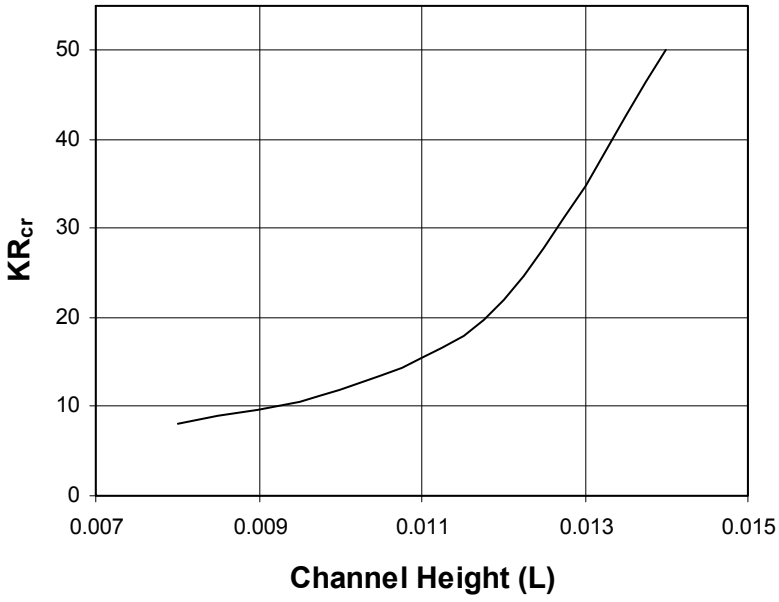


**Fig. 10.**

**Table. 1.** Grid Independence Test for Fluid Annulus

| Parameters | | Fluid-Annulus Mesh (N x M) | | | | | |
|---|---|---|---|---|---|---|---|
| | | **20x20** | **20x25** | **25x25** | **25x30** | **30x25** | **30x30** |
| $HF_{i,ex}$ | **Value** | 2.944036 | 2.943998 | 2.946222 | 2.946270 | 2.949074 | 2.949082 |
| | **% Diff.** | 0.171 | 0.172 | 0.097 | 0.095 | 0.000 | |
| $HF_{o,ex}$ | **Value** | -1.468238 | -1.468204 | -1.467074 | -1.467037 | -1.465612 | -1.465601 |
| | **% Diff.** | 0.180 | 0.178 | 0.101 | 0.098 | 0.001 | |
| $NU_{i,ex}$ | **Value** | 5.054928 | 5.054663 | 5.050683 | 5.050607 | 5.048941 | 5.048845 |
| | **% Diff.** | 0.120 | 0.115 | 0.036 | 0.035 | 0.002 | |
| $NU_{o,ex}$ | **Value** | 3.515973 | 3.516085 | 3.520960 | 3.521028 | 3.523932 | 3.524012 |
| | **% Diff.** | 0.228 | 0.225 | 0.087 | 0.085 | 0.002 | |
| $\theta_{m,ex}$ | **Value** | 0.417591 | 0.417568 | 0.416669 | 0.416650 | 0.415902 | 0.415890 |
| | **% Diff.** | 0.409 | 0.403 | 0.187 | 0.183 | 0.003 | |
| **Time (min.)** | **Value** | 4.902995 | 7.642838 | 13.014520 | 21.750520 | 22.525000 | 35.345510 |
| | **% ratio** | 13.872 | 21.623 | 36.821 | 61.537 | 63.728 | |

**Table.2.** Comparison With Available Results For Eccentric Annuli

**CONFIGURATION**

$NR_1$=0.499 N = 20

$NR_2$=0.5 M = 20

$NR_4$=1.002 NSI = 8

KR=1000 NSO = 16

E=0.6 Case = 1.I

Pr=0.7 Forced Convection

| Parameters/Models | Present | El-Shaarawi& Haider [17] | % error | Present | Shah and London [20] | % error |
|---|---|---|---|---|---|---|
| $(dp/dz)_{fd}$ | 32.2466 | 32.2070 | 0.1229 | 32.2466 | 31.8180 | 1.3470 |
| | **Present** | **El-Shaarawi& Haider [17]** | **% error** | **Present** | **Trombetta [10]** | **% error** |
| $HF_{i,fd}$ | 3.5948 | 3.5930 | 0.0500 | 3.5948 | 3.5820 | 0.3573 |
| $AVNU_{i,fd}$ | 5.7407 | 5.7380 | 0.0468 | 5.7407 | 5.7460 | 0.0925 |
| $AVNU_{o,fd}$ | 4.7616 | 4.7620 | 0.0077 | 4.7616 | 4.7540 | 0.1606 |

**Table. 3.** Radius Ratios for Standard Steel Pipes

| Nominal Size (Inch) | | Radius Ratio | | | | Dimensionless Tube Thickness | |
|---|---|---|---|---|---|---|---|
| Inner | Outer | ASTM Schedule # | $NR_1$ | $NR_2$ | $NR_4$ | Inner | Outer |
| 1/4 | 1 | Sch. 40 | 0.35 | 0.51 | 1.25 | 0.17 | 0.25 |
| | | Sch. 80 | 0.32 | 0.56 | 1.37 | 0.25 | 0.37 |
| 3/8 | 1 ¼ | Sch. 40 | 0.36 | 0.49 | 1.2 | 0.13 | 0.2 |
| | | Sch. 80 | 0.33 | 0.53 | 1.3 | 0.2 | 0.3 |
| 1/2 | 1 ½ | Sch. 40 | 0.39 | 0.52 | 1.18 | 0.14 | 0.18 |
| | | Sch. 80 | 0.36 | 0.56 | 1.27 | 0.2 | 0.27 |
| 3/4 | 2 | Sch. 40 | 0.4 | 0.51 | 1.15 | 0.11 | 0.15 |
| | | Sch. 80 | 0.38 | 0.54 | 1.22 | 0.16 | 0.22 |
| 1 | 2 ½ | Sch. 40 | 0.42 | 0.53 | 1.16 | 0.11 | 0.16 |
| | | Sch. 80 | 0.41 | 0.57 | 1.24 | 0.15 | 0.24 |
| 1 ½ | 4 | Sch. 40 | 0.4 | 0.47 | 1.12 | 0.07 | 0.12 |
| | | Sch. 80 | 0.39 | 0.5 | 1.18 | 0.1 | 0.18 |

**Table. 4.** Common Values of KR

| Material | Thermal Conductivity (W/m-$^0$C) |
|---|---|
| Air @ 300 K | 0.02624 |
| Carbon Steel (1 % C) | 43 |
| Water - Saturated @ 300 K | 0.613 |
| Cast Iron (4 % C) @ 293 K | 52 |
| Engine Oil (SAE 50) @ 293 K | 0.145 |
| Aluminum Metal @ 293 K | 236 |
| Asbestos @ 273 K | 0.154 |
| Plastic | 0.48 |

| Solid Fluid Conductivity Ratio (KR) | | | |
|---|---|---|---|
| Material / Fluid | Air | Water | Oil |
| Aluminum | 8993.9 | 384.99 | 1627.59 |
| Cast Iron | 1981.71 | 84.83 | 358.62 |
| Steel | 1638.72 | 70.15 | 296.55 |
| Plastic | 18.29 | 0.78 | 3.31 |
| Asbestos | 5.87 | 0.25 | 1.06 |